Intrinsically disordered proteins drive enamel formation via an evolutionarily conserved self-assembly motif

Tomas Wald[a,1,2], Frantisek Spoutil[b,c,1], Adriana Osickova[a,d], Michaela Prochazkova[b,c], Oldrich Benada[a], Petr Kasparek[b], Ladislav Bumba[a], Ophir D. Klein[e,f,g,h], Radislav Sedlacek[b,c], Peter Sebo[a], Jan Prochazka[b,c,3], and Radim Osicka[a,3]

[a]Institute of Microbiology of the Czech Academy of Sciences, v.v.i., 142 20 Prague 4, Czech Republic; [b]Laboratory of Transgenic Models of Diseases, Division of Biogenesis and Biotechnology of Natural Compounds, Institute of Molecular Genetics of the Czech Academy of Sciences, v.v.i., 142 20 Prague 4, Czech Republic; [c]Czech Centre for Phenogenomics, Division of Biogenesis and Biotechnology of Natural Compounds, Institute of Molecular Genetics of the Czech Academy of Sciences, v.v.i., 142 20 Prague 4, Czech Republic; [d]Department of Biochemistry, Faculty of Science, Charles University in Prague, 128 43 Prague 2, Czech Republic; [e]Program in Craniofacial Biology, University of California, San Francisco, CA 94143; [f]Department of Orofacial Sciences, University of California, San Francisco, CA 94143; [g]Department of Pediatrics, University of California, San Francisco, CA 94143; and [h]Institute for Human Genetics, University of California, San Francisco, CA 94143

Edited by Gerard Karsenty, Columbia University Medical Center, New York, NY, and accepted by Editorial Board Member Peter B. Moore January 17, 2017 (received for review September 15, 2016)

The formation of mineralized tissues is governed by extracellular matrix proteins that assemble into a 3D organic matrix directing the deposition of hydroxyapatite. Although the formation of bones and dentin depends on the self-assembly of type I collagen via the Gly-X-Y motif, the molecular mechanism by which enamel matrix proteins (EMPs) assemble into the organic matrix remains poorly understood. Here we identified a Y/F-x-x-Y/L/F-x-Y/F motif, evolutionarily conserved from the first tetrapods to man, that is crucial for higher order structure self-assembly of the key intrinsically disordered EMPs, ameloblastin and amelogenin. Using targeted mutations in mice and high-resolution imaging, we show that impairment of ameloblastin self-assembly causes disorganization of the enamel organic matrix and yields enamel with disordered hydroxyapatite crystallites. These findings define a paradigm for the molecular mechanism by which the EMPs self-assemble into supramolecular structures and demonstrate that this process is crucial for organization of the organic matrix and formation of properly structured enamel.

ameloblastin | amelogenin | biomineralization | enamel | intrinsically disordered protein

Biomineralization is a key process in vertebrates by which calcium and phosphate ions are incorporated into soft matrices in the form of hydroxyapatite (HAP). The advent of mineralized tissues enabled the evolution of various adaptive phenotypes, such as formation of the endoskeleton, body armor, and teeth (1). Biomineralization depends on evolutionarily related extracellular matrix proteins that control the nucleation and growth of HAP crystallites (2). Most of these proteins are encoded within the 4q13–q21 locus in a large cluster of genes for the secretory calcium-binding phosphoproteins (SCPPs) that have evolved from a common ancestor gene by tandem duplication and neo-functionalization (3–5).

A major competitive advantage of early vertebrates was the evolution of teeth in the oral cavity (6). In tetrapods, teeth are composed of two major mineralized tissues: the relatively softer dentin, produced by odontoblasts of neuroectodermal origin, and the harder enamel, produced by ameloblasts derived from oral epithelial cells. Because of a unique combination of hardness and fracture toughness, the enamel provides mechanical, chemical, and biological protection to the tooth. In more primitive tetrapods, the HAP crystallites of enamel are oriented in the direction of ameloblast movement (7). In mammals, however, enamel is more complex, formed by prisms that cluster and change direction abruptly between the inner enamel–dentin junction (EDJ) and the outer enamel surface (8). This complexity can result in various arrangements, such as the Hunter–Schreger bands (HSBs), in which clusters of prisms change their orientation in a zig-zag pattern (9). Such patterning significantly enhances the resistance of enamel to abrasion and pressure.

Proper formation and quality of enamel depend on the secretion of the structural enamel matrix proteins (EMPs) amelogenin (AMEL) and ameloblastin (AMBN). It is thought that AMEL, the most abundant EMP and the proposed crystallization nucleator (10, 11), diverged from AMBN (4) that itself evolved together with other SCPPs from a common ancestor protein, SPARCL-1 (1). AMBN and AMEL belong to a broad family of intrinsically disordered proteins (IDPs) (12–14) that usually interact via locally folded structures formed by short linear motifs rich in hydrophobic amino acid residues (15, 16). Both proteins self-assemble into higher order structures from monomeric subunits (11, 14), similar to type 1 collagen (COL1), the predominant matrix protein of bones and dentin (17). Although it is well established that COL1 self-assembly involves the consecutive Gly-X-Y motif, neither the molecular basis of the self-assembly of AMBN and AMEL into supramolecular structures nor the role of these structures in the formation of properly structured enamel are known.

Here we report the identification of an evolutionarily conserved Y/F-x-x-Y/L/F-x-Y/F motif that is essential for the self-assembly

Significance

Formation of the hardest mineralized tissue in vertebrates, tooth enamel, relies on a unique set of enamel matrix proteins (EMPs). These EMPs assemble into a 3D extracellular organic matrix that directs the deposition of calcium and phosphate ions into hydroxyapatite crystallites. However, the molecular basis of EMP assembly into the organic matrix remains poorly understood. This study shows that self-assembly of the key EMPs, ameloblastin and amelogenin, involves a short linear amino acid motif that is evolutionarily conserved from the first tetrapods to man. Functionality of this motif in ameloblastin is shown to be essential for organization of the enamel organic matrix and for proper organization of hydroxyapatite crystallites into the compact bundles that determine the structure and mechanical resistance of enamel.

Author contributions: T.W., F.S., J.P., and R.O. designed research; T.W., F.S., A.O., M.P., O.B., P.K., L.B., J.P., and R.O. performed research; T.W., F.S., A.O., M.P., O.B., P.K., L.B., J.P., and R.O. analyzed data; and T.W., F.S., O.D.K., R.S., P.S., J.P., and R.O. wrote the paper.

The authors declare no conflict of interest.

This article is a PNAS Direct Submission. G.K. is a Guest Editor invited by the Editorial Board.

[1] T.W. and F.S. contributed equally to this work.

[2] Present address: Department of Orofacial Sciences and Program in Craniofacial Biology, University of California, San Francisco, CA 94143.

[3] To whom correspondence may be addressed. Email: osicka@biomed.cas.cz or jan.prochazka@img.cas.cz.

This article contains supporting information online at www.pnas.org/lookup/suppl/doi:10.1073/pnas.1615334114/-/DCSupplemental.

of AMBN and AMEL. Targeted mutations in mice revealed that AMBN self-assembly is indispensable for the correct formation of the organic matrix of developing enamel, the oriented growth of HAP crystallites, and inhibition of ingrowth of the interprismatic matrix (IPM) into the prismatic structures. This direct in vivo evidence demonstrates that the formation of supramolecular structures of EMPs is essential for formation of highly structured enamel in mammals.

Results

Identification of a Unique Motif Essential for Self-Assembly of AMBN and AMEL. We have recently demonstrated (14) that human AMBN self-associates into ribbon-like supramolecular structures via a short exon 5-encoded segment consisting of residues 36–72 (Fig. 1*A*). To identify residues that account for the self-assembly capacity of AMBN, we constructed AMBN variants with deletions or with glycine substitutions in the segment 36–72 (Fig. 1*A* and Fig. S1*A*). Analysis of the oligomeric status of such altered AMBN variants by size-exclusion chromatography (SEC) then revealed that the AMBN$^{\Delta 54\text{–}72}$, AMBN$^{44\text{–}53\text{-G}}$, and AMBN$^{\text{RK–GG}}$ variants still behaved like intact AMBN and eluted as large molecular mass polymeric species in the void volume of a column with a 1,300 kDa cutoff (Fig. 1*B*). In contrast, the AMBN$^{\Delta 36\text{–}53}$, AMBN$^{36\text{-}43\text{-G}}$, and AMBN$^{\text{YYF–GGG}}$ variants eluted as a sharp peak corresponding to AMBN monomers (Fig. 1*B*). Accordingly, no polymeric structures were observed for these mutant variants by transmission electron microscopy (TEM) (Fig. 1*C*), whereas the AMBN$^{\Delta 54\text{–}72}$, AMBN$^{44\text{–}53\text{–G}}$, and AMBN$^{\text{RK–GG}}$ variants still formed the polymeric ribbons observed with intact AMBN (Fig. 1*C*). Hence, the aromatic residues Tyr^{36}, Tyr^{39}, and Phe^{41}, forming the short linear motif involving residues 36–41, were required for AMBN self-assembly. Indeed, each of the individual glycine substitutions of Tyr^{36}, Tyr^{39}, and Phe^{41} disrupted the capacity of AMBN to oligomerize and form the ribbon-like structures (Fig. 1 *B* and *C*). Hence, the involvement of any of the three aromatic residues was critical for AMBN self-assembly. Moreover, when the segment consisting of residues 36–41 (R$_{36\text{–}41}$) was genetically fused to the monomeric C-terminal domain of AMBN (AMBN-C$_{\text{term}}$) (14), the resulting R$_{36\text{–}41}$–AMBN-C$_{\text{term}}$ fusion protein gained the capacity to form

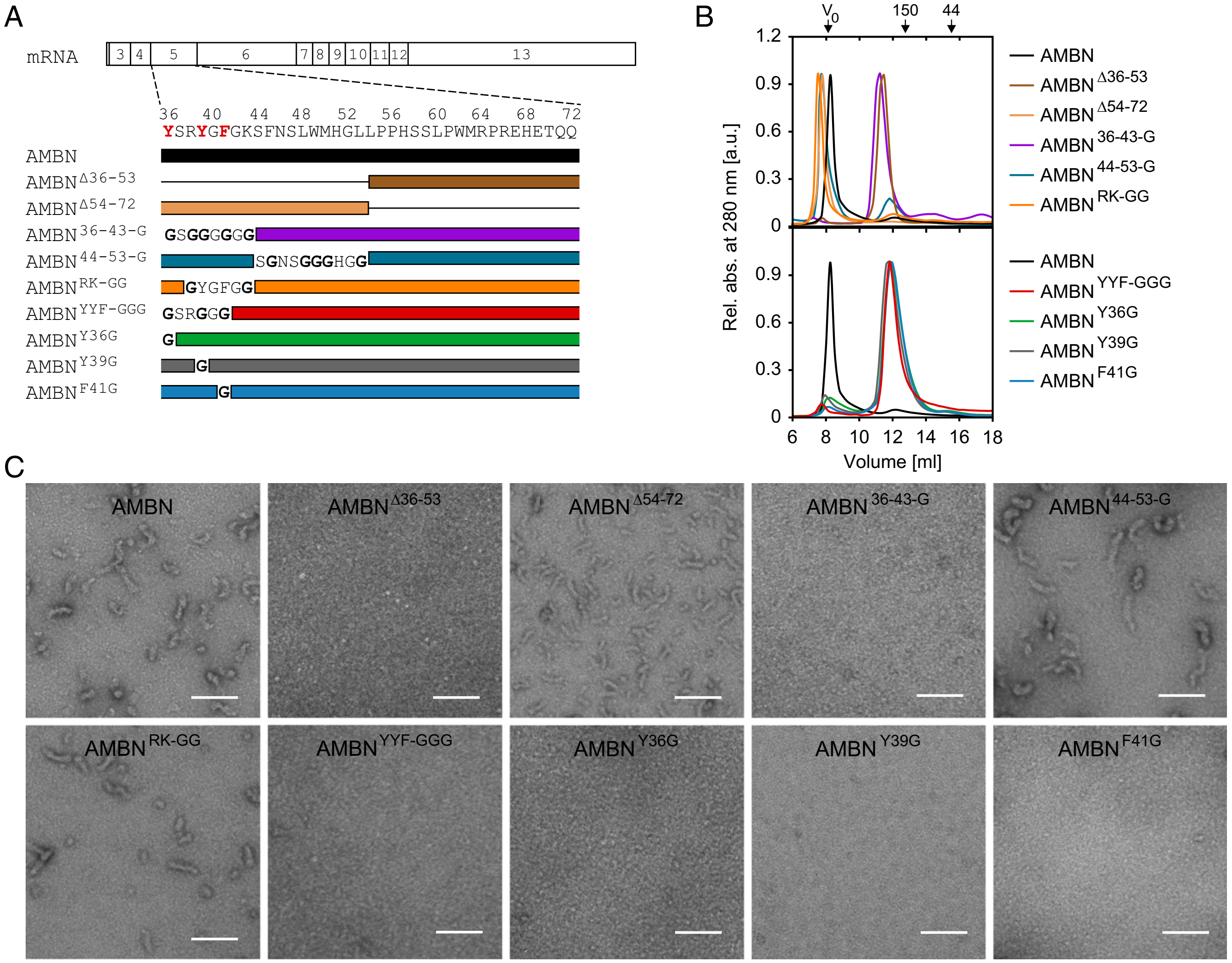

Fig. 1. Identification of residues essential for the self-assembly of AMBN. (*A*) Schematic representations of human *Ambn* mRNA, of the zoomed-out exon 5-encoded sequence comprising residues 36–72 of AMBN, and of the sequence modifications in the mutant AMBN variants. Letters in red represent residues identified as indispensable for AMBN self-assembly. The solid lines replacing the brown-colored bars represent the portions deleted in AMBN. The glycine residues indicated in bold represent the substitutions introduced into the original AMBN sequence. Amino acid numbering is based on the sequence of the mature AMBN protein lacking the secretion signal peptide (AMBN, sequence NP_057603.1). (*B*) Purified recombinant intact AMBN (black line) and its mutant variants (colored lines) were analyzed by SEC on a Superdex 200 10/300 column. The molecular masses of the globular protein standards are indicated in kilodaltons above the chromatograms. V_0, void volume. (*C*) TEM of purified intact AMBN and of its mutant variants. (Primary magnification: 64,000×.) (Scale bars, 100 nm.)

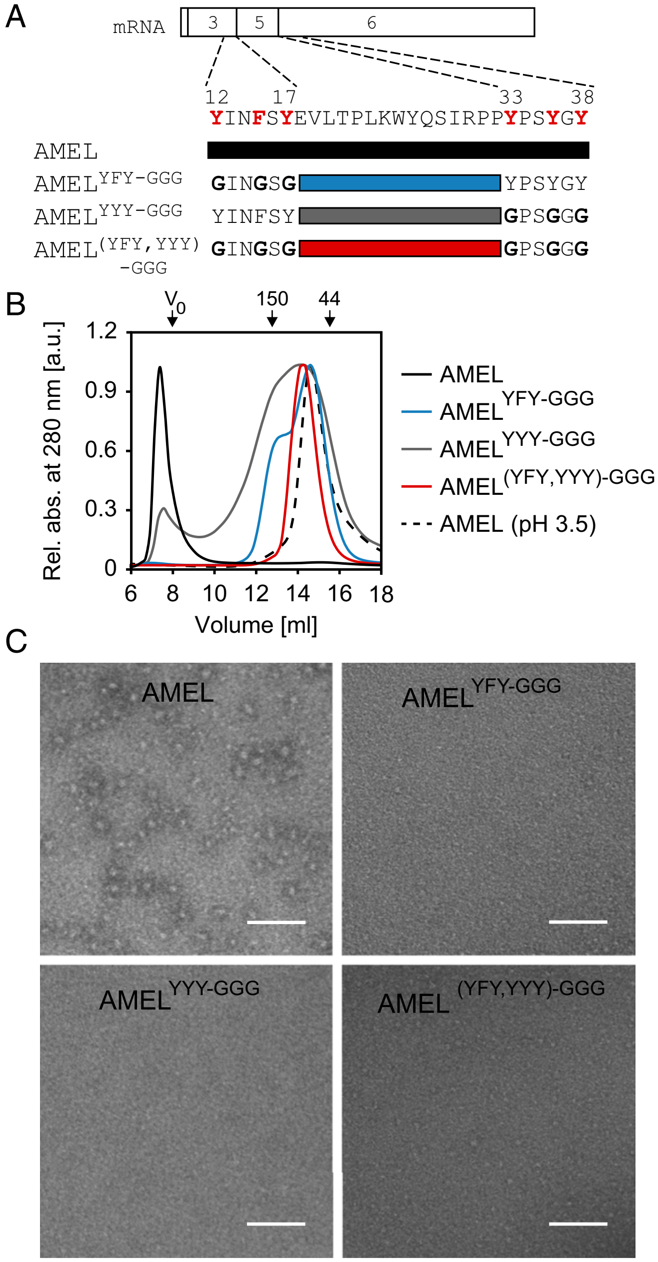

Fig. 2. Identification of residues essential for AMEL self-assembly. (*A*) Schematic representation of human *Amel* mRNA, of the amino acid sequence comprising residues 12–38 of AMEL with mutated segments 12–17 and 33–38, and of the mutant AMEL variants. Letters in red represent residues identified as indispensable for AMEL self-assembly. The glycine residues indicated in bold represent substitutions introduced into the original AMEL sequence. Amino acid numbering is based on the sequence of the mature AMEL protein lacking the secretion signal peptide (AMEL, sequence NP_001133.1). (*B*) Purified recombinant intact AMEL (black line) and its mutant variants (colored lines) were analyzed by SEC on a Superdex 200 10/300 column. The monomeric acid-treated AMEL (20) was used as a control. The molecular masses of the globular protein standards are indicated in kilodaltons above the chromatogram. V_0, void volume. (*C*) TEM of purified intact AMEL and of its mutant variants. (Primary magnification: 64,000×.) (Scale bars, 100 nm.)

ribbon-like supramolecular structures similar to those formed by the entire AMBN (Fig. S2). However, no such structures were observed when the segment R$_{36–41}$ of AMBN was fused to an unrelated intrinsically disordered protein, the self-processing module (SPM) of the bacterial Fe-regulated protein C (FrpC) (Fig. S2) (18, 19). Hence, the AMBN segment comprising residues 36–41 was sufficient to mediate self-assembly of an enamel protein.

In the primary sequence of AMEL, the other major self-assembling EMP, two segments (residues 12–17 and 33–38) resemble the self-assembly motif of AMBN (Fig. 2*A*). To test whether these segments play a role in AMEL self-assembly, the aromatic residues of the first (Tyr^{12}, Phe^{15}, and Tyr^{17}), second (Tyr^{33}, Tyr^{36}, and Tyr^{38}), or both segments were replaced with glycine residues (Fig. 2*A* and Fig. S1*B*). In contrast to native AMEL, which eluted in the void volume of the SEC column as a large oligomer, the applied AMEL$^{\text{YFY–GGG}}$ and AMEL$^{\text{YYY–GGG}}$ variants eluted as broad included peaks, having the monomeric form of the proteins as the predominant component (Fig. 2*B*). Moreover, the AMEL$^{\text{(YFY,YYY)–GGG}}$ construct with glycine substitutions in both segments eluted quantitatively as a narrow peak of the monomeric form (Fig. 2*B*). Accordingly, no complexes were observed with any of the mutant AMEL variants by TEM, whereas the intact AMEL formed the expected polymeric structures (Fig. 2*C*). Hence, the mutated segments were critical for AMEL self-assembly.

To corroborate these observations, the AMBN and AMEL proteins were N-terminally fused to an α-helical tolerance to group A colicins (TolA) protein segment containing 52 Lys residues that

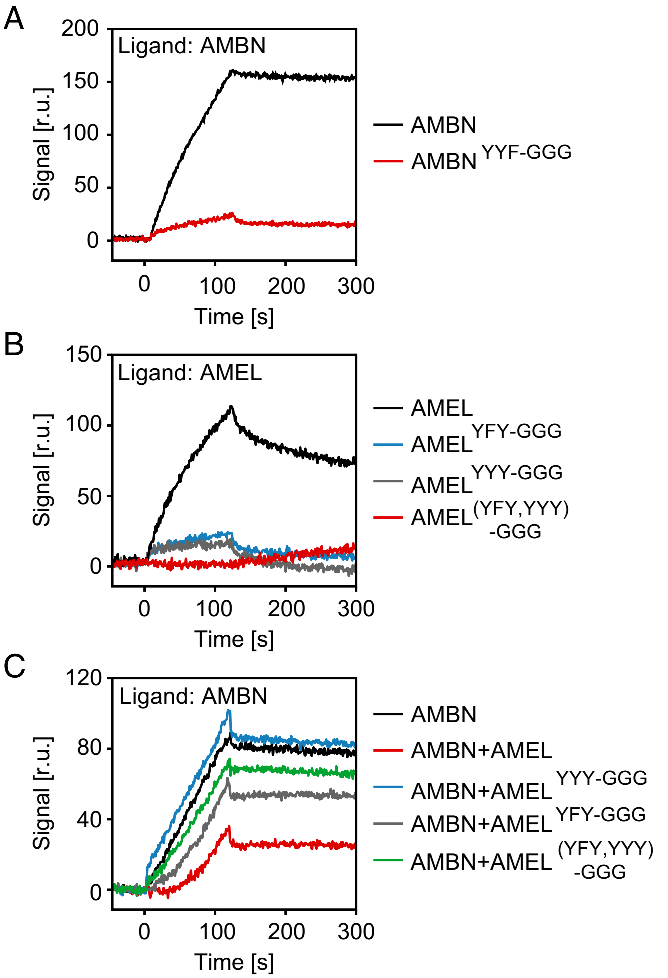

Fig. 3. SPR measurements confirm that the integrity of the self-assembly motif is crucial for the association of AMBN and AMEL. (*A* and *B*) Purified intact AMBN (*A*) or AMEL (*B*) (1.0 μM) and their mutant variants AMBN$^{\text{YYF–GGG}}$ (*A*) or AMEL$^{\text{YFY–GGG}}$, AMEL$^{\text{YYY–GGG}}$, and AMEL$^{\text{(YFY,YYY)–GGG}}$ (*B*) were probed by SPR for binding to the immobilized TolA-AMBN (*A*) or TolA-AMEL (*B*) fusion proteins. (*C*) Binding of intact AMBN to immobilized TolA-AMBN was analyzed in the presence of equimolar amounts of AMEL, AMEL$^{\text{YFY–GGG}}$, AMEL$^{\text{YYY–GGG}}$, or AMEL$^{\text{(YFY,YYY)–GGG}}$.

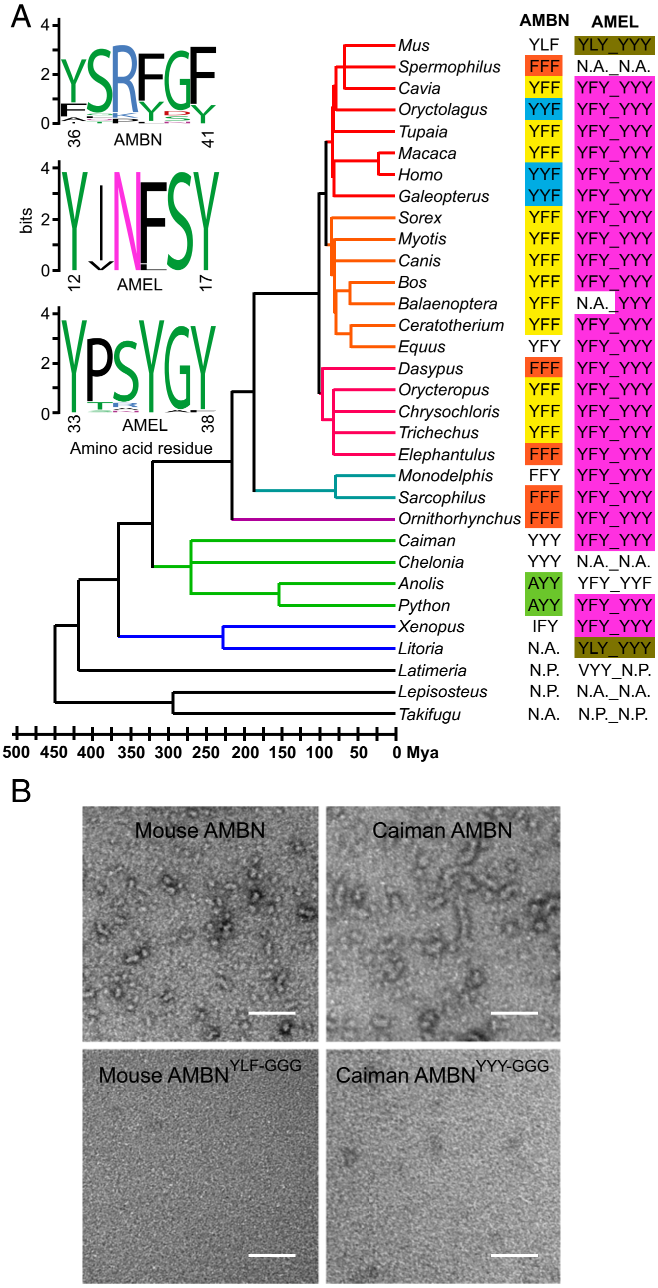

Fig. 4. The self-assembly motif is evolutionarily conserved in tetrapods. (*A*) AMBN and AMEL protein sequences from different species (GenBank accession numbers are listed in Tables S1 and S2) were aligned, and the three key residues of the self-assembly motifs (one in AMBN and two in AMEL) are displayed for each clade of a consensual phylogenic tree of the representative genera of tetrapods (based on refs. 24–27). The self-assembly motifs with the same amino acid sequence within the phylogenetic tree are shown in the same color. N.A., the amino acid sequence was not available; N.P., the self-assembly motif was not present. The three sequence logos in the upper left corner show the conservation of the amino acid residues within the self-assembly motif (one in AMBN, two in AMEL). (*B*) TEM of purified intact AMBN of mouse and caiman and of their corresponding mutant variants with glycine substitutions in the three key residues of the self-assembly motif. (Primary magnification: 64,000×.) (Scale bars, 100 nm.)

enabled oriented and highly efficient immobilization of the AMBN and AMEL proteins to the general layer compact (GLC) surface of surface plasmon resonance (SPR) sensor chips. SPR analysis then revealed that immobilized TolA-AMBN bound the intact AMBN strongly, whereas only residual binding of the AMBN$^{\mathrm{YYF-GGG}}$ variant was observed (Fig. 3*A*). Similarly, immobilized TolA-AMEL bound the intact AMEL strongly, whereas only poor binding of the AMEL$^{\mathrm{YFY-GGG}}$, AMEL$^{\mathrm{YYY-GGG}}$, or AMEL$^{\mathrm{(YFY,YYY)-GGG}}$ variants was detected (Fig. 3*B*). Moreover, binding of intact AMBN to immobilized TolA-AMBN was strongly reduced in the presence of equimolar amounts of intact AMEL but was impaired only partly or not at all in the presence of the AMEL$^{\mathrm{YFY-GGG}}$, AMEL$^{\mathrm{YYY-GGG}}$, or AMEL$^{\mathrm{(YFY,YYY)-GGG}}$ variants, respectively (Fig. 3*C*). All these data demonstrate that the integrity of the self-assembly motif defined here determines the capacity of AMBN and AMEL to form large polymeric structures and may be important for the previously described interaction between AMBN and AMEL (21–23).

The Self-Assembly Motif of EMPs Is Evolutionarily Conserved in Tetrapods. We next asked whether the self-assembly motif of EMPs is evolutionarily conserved among vertebrates. Therefore, we aligned the GenBank-deposited sequences of AMBN and AMEL proteins from different species (Tables S1 and S2) and displayed the three key residues of the self-assembly motifs for each corresponding clade of a consensual phylogenic tree for the representative vertebrate genera (Fig. 4*A*). Interestingly, the aromatic tyrosine and/or phenylalanine residues were found to be evolutionarily conserved in all three key positions of the self-assembly motifs of almost all aligned EMP sequences of tetrapods (Fig. 4*A*). The randomly and rarely occurring aliphatic hydrophobic residues thus point to the importance of maintaining of overall hydrophobicity of the self-assembly motif, which may reflect the intrinsically disordered nature of the EMPs. In contrast, the self-assembly motif was not present in ray-finned (Actinopterygii) and lobe-finned (Sarcopterygii) fish (Fig. 4*A*).

To corroborate that the function of the self-assembly motif is conserved across tetrapods, we produced the AMBN proteins of mouse and caiman that diverged ∼300 million years ago. Indeed, the intact AMBN proteins of both species self-assembled into polymeric structures (Fig. 4*B*), whereas their capacity to polymerize was disrupted when the key residues of the self-assembly motif (i.e., Tyr^{41}, Leu^{44}, and Phe^{46} in mouse AMBN$^{\mathrm{YLF-GGG}}$ and Tyr^{34}, Tyr^{37}, and Tyr^{39} in caiman AMBN$^{\mathrm{YYY-GGG}}$) were replaced by glycine (Fig. 4*B*). These data define a self-assembly motif with the consensus sequence Y/F-x-x-Y/L/F-x-Y/F, which is common to major EMPs. This motif appears to be functionally conserved from the early stages of tetrapod evolution and thus is likely of high importance in enamel formation.

Self-Assembly of AMBN Is Crucial for the Formation of Highly Structured Enamel. To examine the biological role of the self-assembly motif in enamel formation, we generated a mutant *Ambn*$^{G/G}$ mouse producing AMBN in which the three residues of the self-assembly motif (Tyr^{41}, Leu^{44}, and Phe^{46}) were replaced by glycine residues (Fig. 5 *A*–*C* and Fig. S3). As a model of *Ambn* loss of function, we further generated a mutant *Ambn*$^{-/-}$ mouse with an 8-bp deletion at the 5′ end of *Ambn* exon 5 that yielded a frameshift introducing a stop codon (Fig. 5*C* and Fig. S3*A*). Comparable *Ambn* mRNA and AMBN protein levels were detected in preameloblasts and early ameloblasts of *Ambn*$^{WT/WT}$ and *Ambn*$^{G/G}$ mice, whereas only background *Ambn* mRNA levels were detected and no AMBN protein was produced by *Ambn*$^{-/-}$ mice (Fig. 5 *D* and *E*).

To confirm that the disruption of the self-assembly motif also yielded monomeric AMBN in vivo, incisor cervical loops of the wild-type and *Ambn*$^{G/G}$ mice were extracted, and the oligomeric state of AMBN was analyzed by sedimentation through glycerol gradients. Although most of the AMBN extracted from incisors of *Ambn*$^{WT/WT}$ mice was found in the denser fractions 4 and 5 of the gradient (Fig. 5*F*), the extracted AMBN^{G} sedimented more slowly, and most of it was present in the lighter fractions 2 and 3 of the gradient (Fig. 5*F*). Hence the AMBN^{G} protein was defective in forming the large and more rapidly sedimenting oligomeric structures within the enamel matrix of *Ambn*$^{G/G}$ mice.

Examination by microcomputed tomography (μCT) (Fig. 6 *A*–*F*) and SEM (Fig. 6 *G*–*I*) revealed that the incisors of *Ambn*$^{G/G}$ mice were covered by an aberrantly formed enamel layer (Fig. 6 *B*, *E*, and

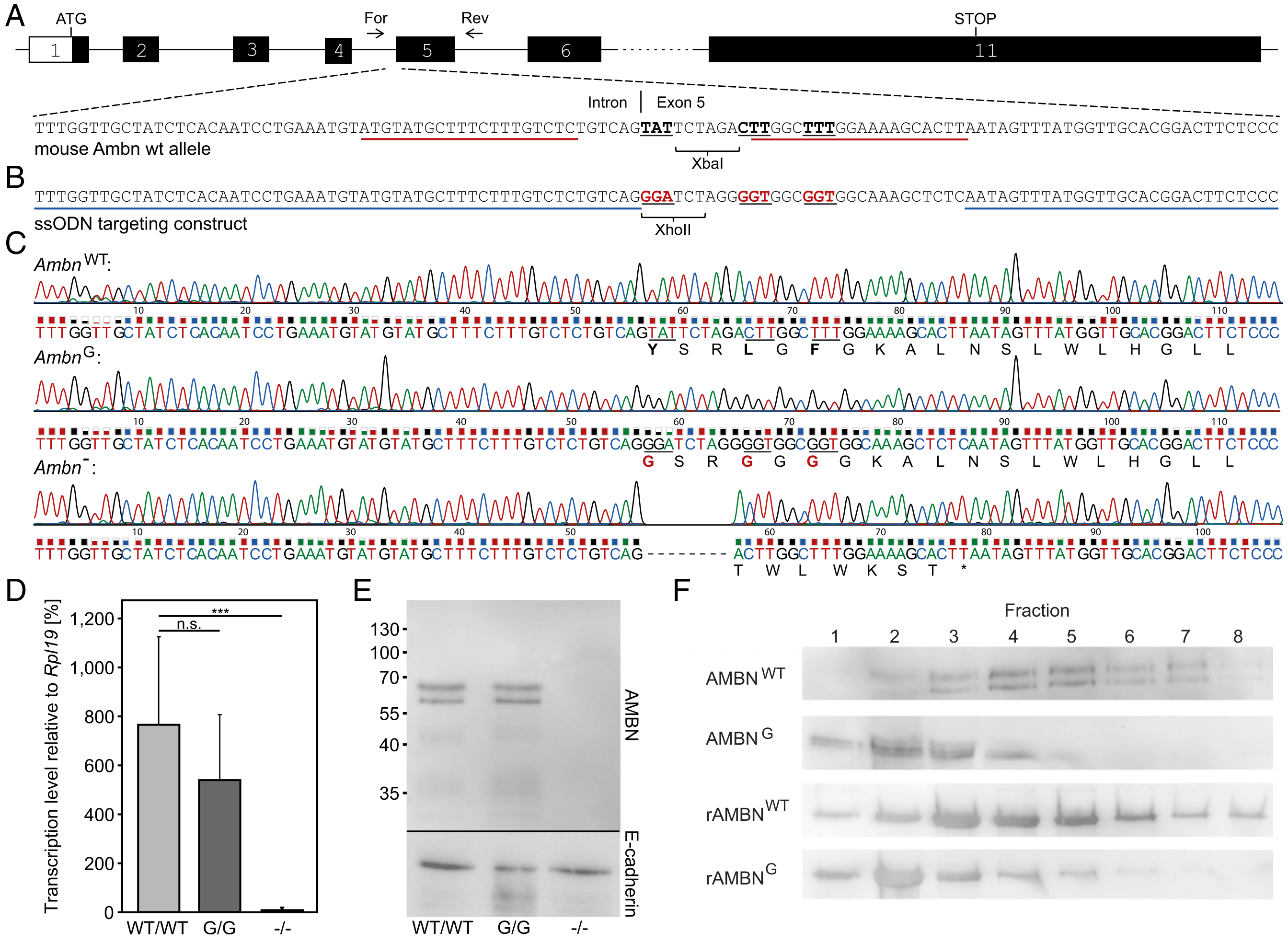

Fig. 5. Construction and analysis of *Ambn*^{G} and *Ambn*$^{-}$ alleles. (*A*) Schematic representation of the mouse *Ambn* gene with depiction of the targeted DNA sequence. Codons for the three key residues of the self-assembly motif are shown as underlined bold characters. TALEN-binding sites are underlined in red. (*B*) The *Ambn*-targeting single-stranded oligodeoxynucleotide (ssODN) with the sequences homologous to the *Ambn* gene is underlined in blue, and the glycine codons replacing the codons for the three key residues of the self-assembly motif are shown in bold red and are underlined. The ssODN was designed with silent mutations within the recognition sequence of *Ambn*-TALEN to avoid repetitive digestions. (*C*) Chromosomal DNA samples extracted from the tails of targeted mice were used as templates for PCR reactions with primers For and Rev (*A*), and the amplified products were examined by restriction analysis using XbaI (*A*) and XhoII (*B*) endonucleases (Fig. S3*A*) and by DNA sequencing. The resulting chromatograms of the *Ambn*^{WT}, *Ambn*^{G}, and *Ambn*$^{-}$ alleles encompassing the mutated region are shown. Partial amino acid sequences encoded by exon 5 of the *Ambn*^{WT}, *Ambn*^{G}, and *Ambn*$^{-}$ alleles are shown below each chromatogram. The three key amino acid residues of the self-assembly motif are shown in bold (*Ambn*^{WT}), and the introduced glycine residues are shown in bold red (*Ambn*^{G}). The 8-bp deletion (dashed line) in exon 5 of the *Ambn*$^{-}$ allele causes a frame-shift introducing a STOP codon (asterisk). (*D*) Relative expression levels of *Ambn* mRNA in the lower incisors of *Ambn*$^{WT/WT}$, *Ambn*$^{G/G}$, and *Ambn*$^{-/-}$ mice were analyzed by quantitative PCR (qPCR) and were normalized to *Rpl19*. The bars represent the mean values with the SD from at least three independent specimens measured in triplicate (n.s., $P > 0.05$; $^{***}P < 0.001$). (*E*) Western blot analysis of AMBN production in the lower incisors of *Ambn*$^{WT/WT}$, *Ambn*$^{G/G}$, and *Ambn*$^{-/-}$ mice. E-cadherin was used as a loading control. Molecular masses in kilodaltons are given on the left side of the panel. (*F*) Cervical loops from mouse lower incisors were isolated, and the proteins were separated by glycerol gradient ultracentrifugation. Western blot analysis of the AMBN distribution demonstrates that AMBN isolated from *Ambn*$^{WT/WT}$ mouse incisors forms polymeric structures that sediment similarly as the recombinant AMBN protein (rAMBN^{WT}). In contrast, AMBN isolated from *Ambn*$^{G/G}$ mouse incisors remains monomeric, similar to the mutant monomeric recombinant AMBN protein (rAMBN^{G}).

H) that differed significantly in structure from the normal enamel of *Ambn*$^{WT/WT}$ mice (Fig. 6 *A*, *D*, and *G*). X-ray absorption intensities revealed reduced mineralization of the enamel of *Ambn*$^{G/G}$ mice compared with *Ambn*$^{WT/WT}$ mice (Fig. 6*J*). Concurrently, energy-dispersive X-ray spectroscopy (EDS) analysis of the mineral composition showed that the enamel of *Ambn*$^{G/G}$ mice contained slightly lower amounts of calcium and phosphorus and higher amounts of carbon than the enamel of *Ambn*$^{WT/WT}$ mice (Fig. 6 *K*, *L*, and *M*), indicating a higher content of residual protein in the enamel of *Ambn*$^{G/G}$ mice. Production of the triply substituted AMBN^{G} variant still allowed the formation of an enamel layer of normal thickness (Fig. 6 *B*, *E*, *H*, and *N*). In contrast, only a residual mineral layer was formed on incisors of *Ambn*$^{-/-}$ mice in the absence of the AMBN protein (Fig. 6 *C*, *F*, *I*, and *N*), although the dentin part remained unaffected (Fig. 6*O*). These data indicate that the self-assembly motif of AMBN is not involved in the control of enamel thickness but instead plays a role in determining enamel structure.

The substantial alteration of enamel structure was, indeed, observable by SEM on acid-etched *Ambn*$^{G/G}$ mouse incisors, even at low magnification (Fig. 7 *A* and *B* and stereoscopic images in Fig. S4 *A* and *C*). In contrast to the normal enamel of *Ambn*$^{WT/WT}$ mice, which is characterized by a well-organized structure of uniserial HSBs (Fig. 7*A* and Fig. S4*A*), the enamel of *Ambn*$^{G/G}$ mice exhibited a simple radial organization without visible HSBs (Fig. 7*B* and Fig. S4*C*). At higher magnification striking differences in the structure of individual HAP crystallites were observed (Fig. 7 *D* and *E* and Fig. S4 *B* and *D*). In the enamel of normal mice, the crystallites were arranged regularly in tightly packed bundles,

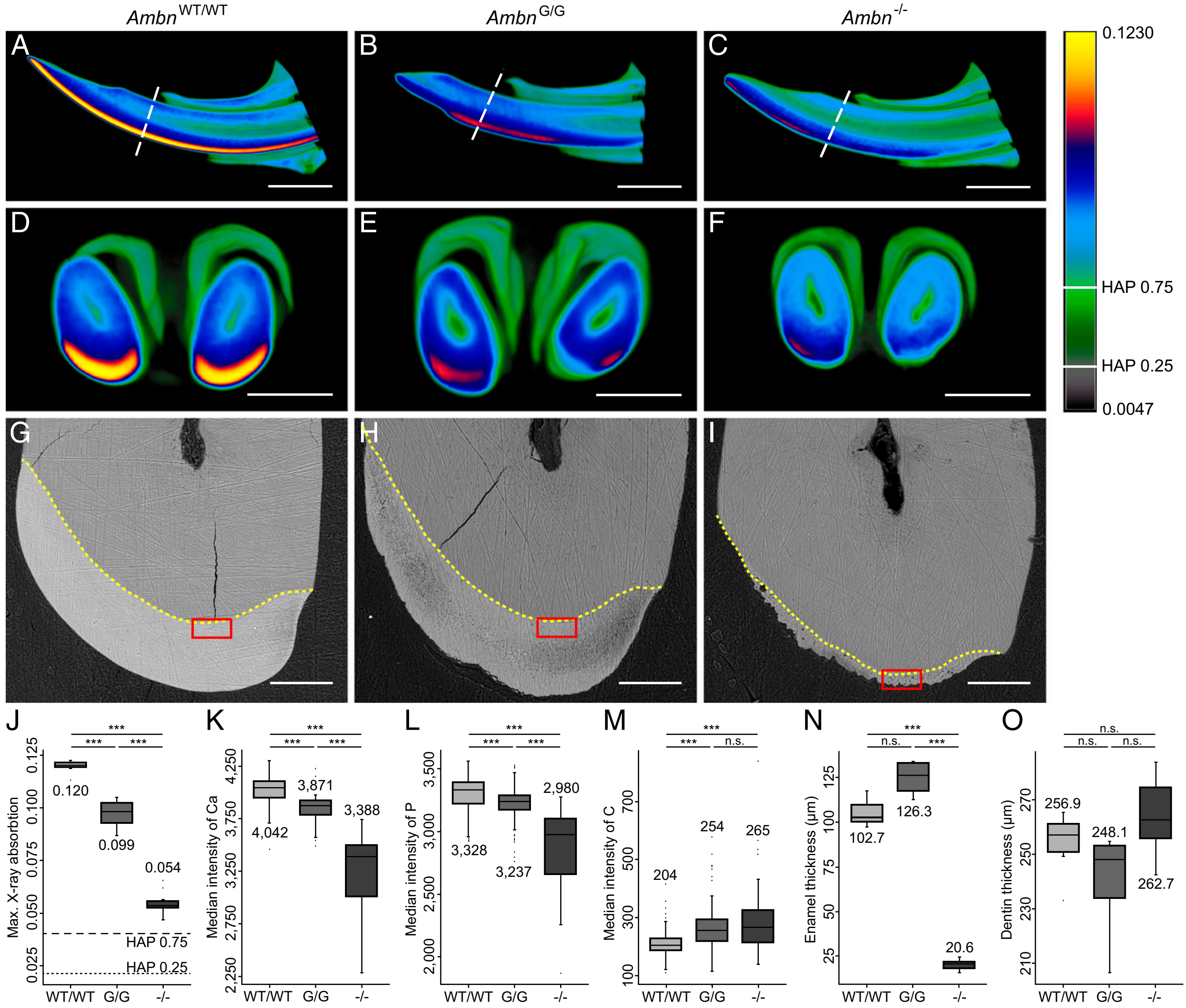

Fig. 6. Self-assembly of AMBN is required for enamel mineralization. (*A*–*F*) MicroCT and (*G*–*I*) SEM images of incisor enamel of *Ambn*$^{WT/WT}$ (*A*, *D*, and *G*), *Ambn*$^{G/G}$ (*B*, *E*, and *H*), and *Ambn*$^{-/-}$ (*C*, *F*, *I*) mice. (*A*–*C*) Virtual longitudinal µCT sections through the lower incisors. The range of pseudocolors is displayed with highlighted values for 25% and 75% HAP phantoms. The dashed line marks positions of virtual sections (*D*–*F*). One representative experiment of three (*Ambn*$^{WT/WT}$ and *Ambn*$^{G/G}$) or five (*Ambn*$^{-/-}$) performed is shown in each panel. (Scale bars, 1 mm.) (*D*–*F*) Frontal virtual sections through lower incisors in the positions marked in *A*–*C*. One representative experiment of three (*Ambn*$^{WT/WT}$ and *Ambn*$^{G/G}$) or five (*Ambn*$^{-/-}$) performed is shown in each panel. (Scale bars, 500 µm.) (*G*–*I*) SEM of unetched enamel layers of frontal sections of lower right incisors (buccal side on the left). The images were acquired by a concentric backscattered detector. (Primary magnification: 500×.) The yellow dotted line represents the EDJ, and the red box delineates the area selected for EDS. One representative experiment of four (*Ambn*$^{WT/WT}$ and *Ambn*$^{-/-}$) or three (*Ambn*$^{G/G}$) performed is shown in each panel. (Scale bars, 100 µm.) (*J*–*O*) Quantification of enamel parameters in *Ambn*$^{WT/WT}$, *Ambn*$^{G/G}$, and *Ambn*$^{-/-}$ mice represented by box-and-whisker plots with indicated levels of significance (n.s., $P > 0.05$; ***$P < 0.001$). The line within the box represents the median; the box represents the SD; whiskers represent 1.5× the interquartile range; dots represent outliers. The median values are given below or above the boxes. (*J*) Maximum intensity corresponding to the degree of mineralization of enamel region in the virtual µCT sections shown in *D*–*F*. The values were calculated from lower left and right incisors of three *Ambn*$^{WT/WT}$, three *Ambn*$^{G/G}$, and five *Ambn*$^{-/-}$ mice. The dashed line indicates the value for the 75% HAP phantom; the dotted line indicates the value for the 25% HAP phantom. (*K*–*M*) Median intensities of calcium (*K*), phosphorus (*L*), and carbon (*M*) estimated by EDS in the areas marked by the red boxes in *G*–*I* and calculated from the lower right incisors of three *Ambn*$^{WT/WT}$, three *Ambn*$^{G/G}$, and two *Ambn*$^{-/-}$ mice (three linescans were taken for each tooth). See the positive correlation between the maximum intensity from µCT reconstruction and the amount of calcium and phosphorus and the negative correlation between maximum intensity and the amount of carbon. (*N* and *O*) Enamel thickness in the apical area of frontal SEM sections (*N*) and dentin thickness between the pulp and EDJ in the apical area of frontal SEM sections (*O*) calculated for the incisors of three *Ambn*$^{WT/WT}$, three *Ambn*$^{G/G}$, and four *Ambn*$^{-/-}$ mice.

forming prisms and IPM (Fig. 7*D* and Fig. S4*B*), whereas in the enamel of *Ambn*$^{G/G}$ mice the crystallites were ordered irregularly, in bundles that lost compactness (Fig. 7*E* and Fig. S4*D*). The disruption of the self-assembly motif yielded further expansion of IPM at the expense of the prismatic structures (Fig. 7 *B*, *E*, *G*, and *H*). Finally, the enamel of *Ambn*$^{-/-}$ mice consisted of a thin, amorphous, enamel-like crust devoid of any visible higher organization of HAP crystallites (Fig. 7 *C* and *F* and Fig. S4 *E* and *F*). These results thus provide in vivo evidence that the self-assembly of AMBN into supramolecular structures is essential for the formation of correctly structured enamel.

Impairment of AMBN Self-Assembly Causes Disorganization of Enamel Matrix. Despite the striking structural defects of the enamel in the

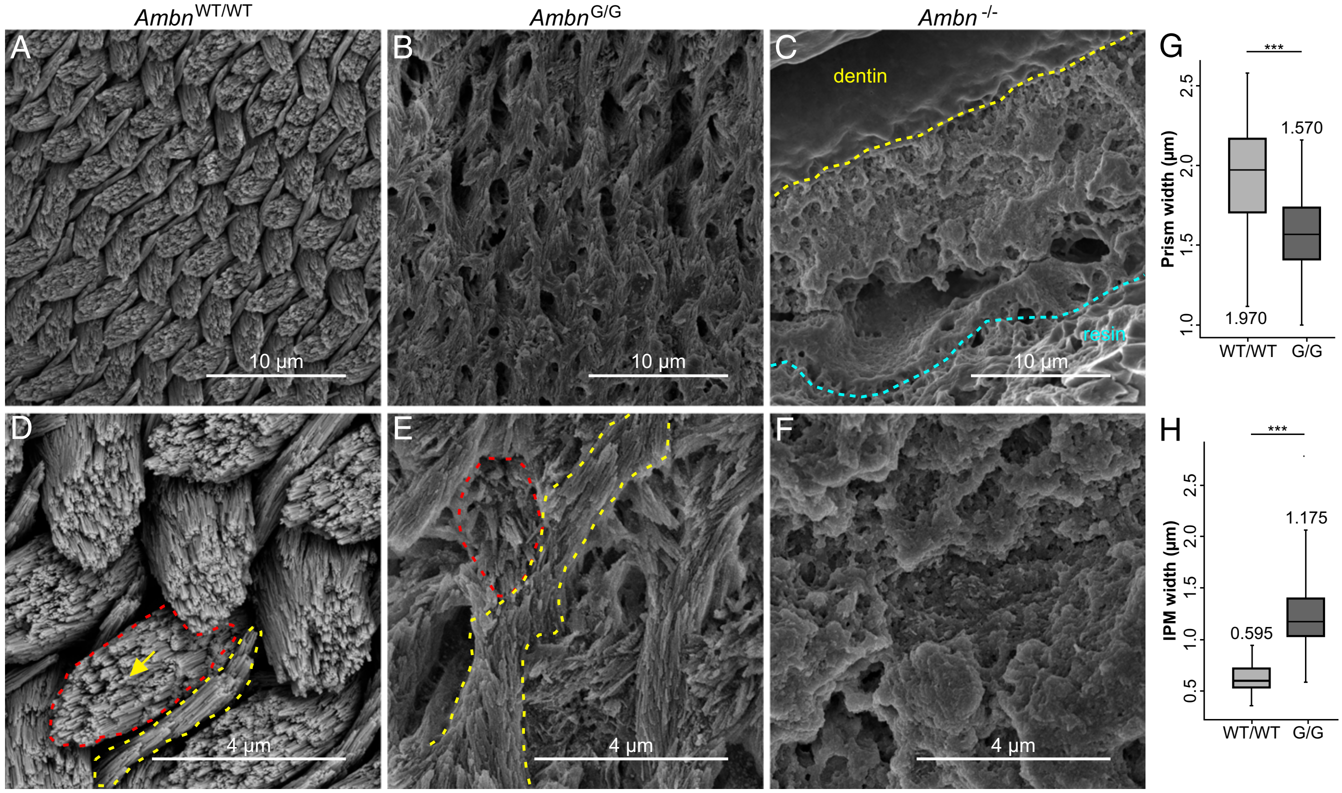

Fig. 7. Self-assembly of AMBN determines the organization of enamel crystallites. (*A*–*F*) SEM images of frontal sections of the lower incisors of *Ambn*$^{WT/WT}$ (*A* and *D*), *Ambn*$^{G/G}$ (*B* and *E*), and *Ambn*$^{-/-}$ (*C* and *F*) mice. (Primary magnification: 10,000× in *A*–*C*; 35,000× in *D*–*F*.) The yellow dotted line in *C* represents the EDJ; the blue dashed line represents the outer enamel surface. Prismatic sheaths in *D* and *E* are indicated by red dotted lines, and the IPM is indicated by yellow dotted lines. The yellow arrow indicates individual HAP crystallites. (*G* and *H*) Prism width (*G*) and IPM width (*H*) calculated from the frontal SEM sections of three *Ambn*$^{WT/WT}$ and three *Ambn*$^{G/G}$ mice.

Ambn$^{G/G}$ mice, no differences in localization and polarization of ameloblasts were observed between *Ambn*$^{WT/WT}$ mice (Fig. 8 *A* and *D*) and *Ambn*$^{G/G}$ mice (Fig. 8 *B* and *E*), and the ameloblasts developed Tomes' processes (Fig. S5). As further shown in Fig. 8, the numbers of ameloblasts (Fig. 8*G*) and odontoblasts (Fig. 8*H*) and the thickness of preenamel (Fig. 8*I*) and predentin (Fig. 8*J*) layers of incisors were similar in *Ambn*$^{WT/WT}$ and *Ambn*$^{G/G}$ mice. In addition, no significant differences in mRNA expression levels of the ameloblast differentiation markers *Shh* (Fig. 8*K*), *Amel* (Fig. 8*L*), and *Mmp20* (Fig. 8*M*) were observed in *Ambn*$^{WT/WT}$ and *Ambn*$^{G/G}$ mice. Moreover, the AMBN and AMEL proteins were still secreted into the extracellular enamel matrix of *Ambn*$^{G/G}$ mice (Fig. S6). However, the AMBN and AMEL proteins were deposited without any obvious pattern in the matrix containing the monomeric AMBN^{G} protein (Fig. 8 *O* and *R*), whereas organized mesh-like structures were observed in the enamel matrix of wild-type mice (Fig. 8 *N* and *Q*). Finally, no AMBN protein was produced by ameloblasts of *Ambn*$^{-/-}$ mice (Fig. 8*P* and Fig. S6*C*), and AMEL secreted into the enamel matrix lacking AMBN formed an unstructured layer of limited thickness (Fig. 8*S* and Fig. S6*H*). Hence the presence and self-assembly capacity of AMBN are critical for formation of the highly organized enamel matrix, which is an essential prerequisite for formation of prismatic enamel in mammals.

Discussion

Hard tissue formation relies on proteins that govern calcium phosphate homeostasis by controlling calcium phosphate stabilization, precipitation, mineral nucleation, and hierarchical HAP assembly (1, 3, 5). These proteins are often partially or fully intrinsically disordered, allowing them to undergo dynamic macromolecular interactions and form an organic matrix scaffold for subsequent biomineralization (28–30). Correct formation of the scaffold usually requires proteolytic cleavage of matrix proteins and their self-assembly into higher order structures. For example, the self-assembly process of collagen, a major organic structural constituent of bone and dentine, depends on the repeating Gly-X-Y amino acid motif. Mutations in this motif cause structural abnormalities, resulting in osteogenesis imperfecta (31). Similarly, the proposed nucleator of HAP deposition in bones and dentin, dentin matrix protein (DMP-1), self-assembles into polymeric structures via the interaction of two specific acidic clusters including residues ESQES and QESQSEQDS (32).

Previously, we and others have shown that the major EMPs, AMBN and AMEL, also possess an intrinsic self-assembly capacity and form higher order structures (11, 14). The first evidence suggesting the existence of a specific sequence responsible for EMP self-assembly revealed that deletion of the segment Met^{1}–Trp^{44} of AMEL abrogates its ability to self-assemble into higher order structures (33). Subsequently, disrupted boundaries between prisms and IPM were observed in the enamel of transgenic mice overexpressing AMEL devoid of the Met^{1}–Trp^{44} segment (34). More recently, the self-assembly capacity of a synthetic peptide consisting of residues 8–21 of AMEL was demonstrated (35), and we recently have shown that the self-assembly capacity of the AMBN protein is determined by the exon 5-encoded segment comprising residues 36–72 (14). Finally, it was shown that production of an incomplete AMBN that lacks the segments encoded by exons 5 and 6 (residues 41–157) results in dental and junctional epithelium defects that abolish structured enamel formation (36). We now report the discovery and functional analysis of an evolutionarily conserved Y/F-x-x-Y/L/F-x-Y/F motif that appears to be indispensable for the self-assembly of the AMBN (residues 36–41) and AMEL (residues 12–17 and 33–38) proteins into higher order structures. This motif is located

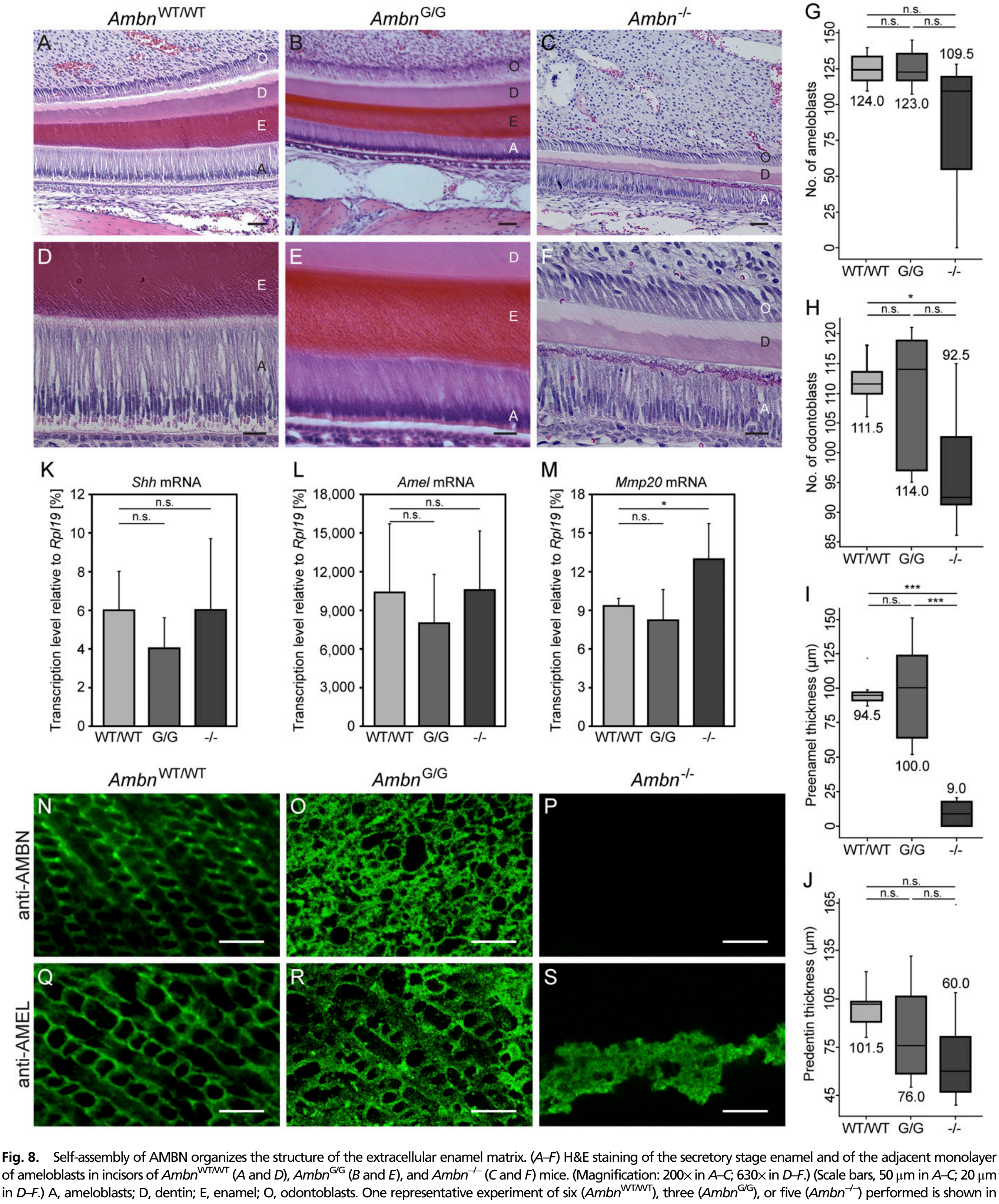

Fig. 8. Self-assembly of AMBN organizes the structure of the extracellular enamel matrix. (*A*–*F*) H&E staining of the secretory stage enamel and of the adjacent monolayer of ameloblasts in incisors of *Ambn*$^{WT/WT}$ (*A* and *D*), *Ambn*$^{G/G}$ (*B* and *E*), and *Ambn*$^{-/-}$ (*C* and *F*) mice. (Magnification: 200× in *A*–*C*; 630× in *D*–*F*.) (Scale bars, 50 μm in *A*–*C*; 20 μm in *D*–*F*.) A, ameloblasts; D, dentin; E, enamel; O, odontoblasts. One representative experiment of six (*Ambn*$^{WT/WT}$), three (*Ambn*$^{G/G}$), or five (*Ambn*$^{-/-}$) performed is shown in each panel. (*G*–*J*) The number of ameloblasts (*G*) and odontoblasts (*H*) and the thickness of preenamel (*I*) and predentin (*J*) calculated from two areas of histological sections of the incisors of three mice of each genetic background. (*K*–*M*) qPCR analysis of mRNA expression of ameloblast differentiation markers *Shh* (*K*), *Amel* (*L*), and *Mmp20* (*M*) in mouse lower incisors. The expression levels of the genes of interest were normalized to the levels of *Rpl19*. The bars represent the mean values plus SD of at least three independent specimens measured in triplicate (n.s., $P > 0.05$; $^{*}P < 0.05$). (*N*–*S*) High-resolution confocal images of AMBN (*N*–*P*) and AMEL (*Q*–*S*) in enamel organic matrix. (Magnification: 1,000×.) (Scale bars, 10 μm.) (*N* and *Q*) Staining of AMBN (*N*) and AMEL (*Q*) in the enamel matrix in the secretory stage of *Ambn*$^{WT/WT}$ ameloblasts. (*O* and *R*) Staining of AMBN (*O*) and AMEL (*R*) in the enamel matrix in the early transition phase of *Ambn*$^{G/G}$ ameloblasts. (*P* and *S*) Staining of AMBN (*P*) and AMEL (*S*) in the enamel matrix in the secretory stage of *Ambn*$^{-/-}$ ameloblasts. One representative experiment of five performed is shown in each panel.

in the N-terminal regions of both proteins, which have evolved from a common ancestor (1, 3, 4).

It is thought that formation of the enamel organic matrix depends on cleavage of EMPs by matrix metalloprotease-20, resulting in the release of different protein moieties exhibiting distinct roles and spatial distribution in the matrix (37, 38). The N-terminal moiety of AMBN comprising the self-assembly motif was shown to colocalize with AMEL across the entire growing enamel (23, 39, 40), indicating the role of the two proteins in the organization of the linear growth of HAP crystallites. This role was shown later for AMEL by Fang et al. (11), who demonstrated in vitro that dodecamer assemblies of full-length AMEL stabilize mineral prenucleation clusters and organize them into parallel arrays of linear chains, yielding the formation of crystallite bundles. As shown here, only irregularly ordered crystallites were observed in the enamel of *Ambn*$^{G/G}$ mice that produce a monomeric form of AMBN (Fig. 7). Hence, the self-assembling capacity of AMBN is required for the development of normal enamel containing the regularly arranged crystallites in tightly packed bundles forming prisms and the IPM.

It remains to be deciphered in more detail how exactly AMBN and AMEL form the protein scaffold of developing enamel. Based on the current data, we hypothesize that AMEL assemblies enable mineral prenucleation clusters to fuse and grow into linear chains (11), whereas the higher order structures of the self-assembled AMBN (or most likely its N-terminal moiety) contribute to the oriented growth of the linear chains of AMEL in the 3D space (Fig. S7*A*). This process, resulting in the formation of regular bundles of crystallites within prisms and the IPM, might occur via a direct interaction between AMEL and AMBN (21–23). Moreover, the N-terminal moiety of AMBN was found to concentrate along the prism/IPM boundary and to form a protein sheath around growing prisms (39, 41). Therefore, it was proposed that the N-terminal moiety of AMBN may inhibit the ingrowth of the interprismatic area into the prismatic structures (42). As shown here, production of monomeric AMBN^{G} led to the disorganization of enamel organic matrix and to the formation of irregularly ordered linear crystallites within prisms and the IPM, with extensive expansion of the IPM at the expense of prismatic structures (Figs. 7 and 8 and Fig. S7*B*). AMBN self-assembly thus plays a key role in the formation of regular bundles of crystallites within prisms and the IPM, and in the delineation of IPM from prisms.

In contrast to the N-terminal moiety, the C-terminal moiety of AMBN was previously found to be monomeric, to bind calcium ions, and to concentrate only at the mineralization front (14, 40, 43). The enamel of *Ambn*$^{-/-}$ mice lacking AMBN consisted of a thin, amorphous, enamel-like crust, but the enamel of *Ambn*$^{G/G}$ mice producing monomeric AMBN was still of proper thickness (Fig. 6). Therefore it is plausible to hypothesize that the C-terminal moiety of AMBN may be required for the proper initiation of crystallite formation.

The EMP self-assembly motif appears to be conserved in all tetrapod lineages (Fig. 4) but is absent from the AMBN or AMEL of actinopterygians or sarcopterygians and appears to have first occurred in tetrapods during the evolution of amphibians. This timing suggests that the evolution of the self-assembly motif might have been connected with the movement of tetrapod ancestors from water onto land. Self-assembly would provide an evolutionarily important mechanism regulating the oriented formation of HAP crystallites, thus reflecting the need for enhanced mechanical and chemical resistance of enamel elicited by the new feeding strategies of the first tetrapods.

The self-assembly motif-driven polymerization of AMBN in Archosauria might have been an ancestral stage that preceded the organization of mammalian enamel. The self-assembling capacity may have contributed to the delineation of the linearly oriented HAP crystallites, as in recent crocodilians (7, 44). Based on the hypothesis that Tomes' processes evolved in early mammals (7, 44), the change in the secretion surface of ameloblasts may have caused the spatiotemporal distribution of AMBN to become involved in the consolidation of organized enamel prisms instead of enamel columns and to separate them from the IPM. This notion suggests that the evolution of the self-assembly motif of AMBN and AMEL might represent an important preadaptation for the evolution of mammalian prismatic enamel.

As shown here, polymerization of AMBN is needed for the formation of the functional enamel matrix (Fig. 8). This polymerization appears to be a prerequisite for regularly arranged crystallites within prisms and the IPM and for the separation of prisms from the surrounding less mature IPM. Such spatial discrimination of two crystallization processes would enable the formation of relatively resistant structures, such as enamel prisms, and it would keep the surrounding softer IPM accessible for mild mechanical adjustments. The existence of such a temporal shift between prism and IPM was indeed found to be important for accomplishment of perfect occlusion in the dentition of bats (45). The data presented here thus set a paradigm showing that the self-assembly of the major EMPs is a critical molecular mechanism that would underlie the formation of highly organized enamel in tetrapods and of the most complex prismatic enamel in mammals.

Materials and Methods

Detailed methods can be found in *SI Materials and Methods*. All work with animals was approved by the Animal Care Committee of the Institute of Molecular Genetics according to institutional and national guidelines. All AMBN and AMEL protein variants were produced in *Escherichia coli* BL21λ(DE3) cells and were purified from crude cell extracts to homogeneity. The purified proteins were examined by high-resolution SEC on a Superdex 200 10/300 column (GE Healthcare), by TEM using a Philips CM100 electron microscope, and by SPR using a Bio-Rad ProteOn XPR36 protein interaction array system. Mutant *Ambn*$^{G/G}$ and *Ambn*$^{-/-}$ mice were generated by transcription activator-like effector nuclease (TALEN) technology, and their incisors were examined by μCT using a SkyScan 1176 μCT scanner (Bruker), by scanning electron microscopy using a Nova NanoSEM 450 scanning electron microscope (FEI), and by confocal microscopy using a Leica Sp5 confocal microscope. Statistical analyses were performed using GraphPad Prism 6.0 (GraphPad Software) or R 3.1.3 software (the R project for statistical computing) with implied libraries dae, nlme, MASS, and ggplot2. Significant differences are indicated as n.s., $P > 0.05$; $^{*}P < 0.05$; $^{**}P < 0.01$; $^{***}P < 0.001$; and $^{****}P < 0.0001$.

ACKNOWLEDGMENTS. We thank I. Beck and H. Palesova from the Czech Centre for Phenogenomics, Institute of Molecular Genetics for their excellent efforts in generating the targeted mutant mice; S. Kozubova, H. Lukeova, and V. Matouskova for excellent technical help; J. Hugo and J. Nachtigall from Maxdorf Publishing, s.r.o. (maxdorf.com/) for producing the illustrations; I. Bibova, R. Pospisil, and J. Kalivoda for the production of anti-AMBN– and anti-AMEL–specific sera; and Jawid Ahmad for providing a TolA-expressing plasmid. This work was supported by the Institutional Research Projects RVO 61388971 and RVO 68378050 of the Czech Academy of Sciences, v.v.i.; by Projects LM2015064 (Czech National Node to the European Infrastructure for Translational Medicine), LQ1604 NPU II, LM2011032, LM2015040 (Czech Centre for Phenogenomics), OP RDI CZ.1.05/2.1.00/19.0395 (Higher quality and capacity for transgenic models), and LO1509 (Prague Infrastructure for Structural Biology and Metabolomics II) from the Ministry of Education, Youth and Sports of the Czech Republic; by Project UNCE204025/2012 of the Charles University in Prague; by the Operational Program Prague-Competitiveness (CZ.2.16/3.1.00/24023); by the Biotechnology and Biomedicine Centre of the Academy of Sciences and Charles University in Vestec (BIOCEV) (CZ.1.05/1.1.00/02.0109); and by NIH R35-DE026602.

1. Kawasaki K, Suzuki T, Weiss KM (2004) Genetic basis for the evolution of vertebrate mineralized tissue. *Proc Natl Acad Sci USA* 101(31):11356–11361.
2. Gajjeraman S, Narayanan K, Hao J, Qin C, George A (2007) Matrix macromolecules in hard tissues control the nucleation and hierarchical assembly of hydroxyapatite. *J Biol Chem* 282(2):1193–1204.
3. Kawasaki K, Weiss KM (2003) Mineralized tissue and vertebrate evolution: The secretory calcium-binding phosphoprotein gene cluster. *Proc Natl Acad Sci USA* 100(7): 4060–4065.
4. Sire JY, Davit-Béal T, Delgado S, Gu X (2007) The origin and evolution of enamel mineralization genes. *Cells Tissues Organs* 186(1):25–48.
5. Kawasaki K (2011) The SCPP gene family and the complexity of hard tissues in vertebrates. *Cells Tissues Organs* 194(2-4):108–112.
6. Price SA, Hopkins SS, Smith KK, Roth VL (2012) Tempo of trophic evolution and its impact on mammalian diversification. *Proc Natl Acad Sci USA* 109(18):7008–7012.
7. Sander PM (1997) Non-mammalian synapsid enamel and the origin of mammalian enamel prisms: The bottom-up perspective. *Tooth Enamel Microstructure*, eds Koenigswald W, Sander PM (A. A. Balkema, Rotterdam), pp 41–62.
8. Clemens WA (1997) Characterization of enamel microstructure terminology and application of the origins of prismatic structures in systematic analysis. *Tooth Enamel Microstructure*, eds Koenigswald W, Sander PM (A. A. Balkema, Rotterdam), pp 85–112.

9. Martin T (1997) Incisor enamel microstructure and systematics in rodents. *Tooth Enamel Microstructure*, eds Koenigswald W, Sander PM (A. A. Balkema, Rotterdam), pp 163–175.
10. Tarasevich BJ, et al. (2007) The nucleation and growth of calcium phosphate by amelogenin. *J Cryst Growth* 304(2):407–415.
11. Fang PA, Conway JF, Margolis HC, Simmer JP, Beniash E (2011) Hierarchical self-assembly of amelogenin and the regulation of biomineralization at the nanoscale. *Proc Natl Acad Sci USA* 108(34):14097–14102.
12. Delak K, et al. (2009) The tooth enamel protein, porcine amelogenin, is an intrinsically disordered protein with an extended molecular configuration in the monomeric form. *Biochemistry* 48(10):2272–2281.
13. Wald T, et al. (2011) Biophysical characterization of recombinant human ameloblastin. *Eur J Oral Sci* 119(Suppl 1):261–269.
14. Wald T, et al. (2013) Intrinsically disordered enamel matrix protein ameloblastin forms ribbon-like supramolecular structures via an N-terminal segment encoded by exon 5. *J Biol Chem* 288(31):22333–22345.
15. Mészáros B, Tompa P, Simon I, Dosztányi Z (2007) Molecular principles of the interactions of disordered proteins. *J Mol Biol* 372(2):549–561.
16. Das RK, Mao AH, Pappu RV (2012) Unmasking functional motifs within disordered regions of proteins. *Sci Signal* 5(220):pe17.
17. Boot-Handford RP, Tuckwell DS (2003) Fibrillar collagen: The key to vertebrate evolution? A tale of molecular incest. *BioEssays* 25(2):142–151.
18. Osicka R, et al. (2004) A novel "clip-and-link" activity of repeat in toxin (RTX) proteins from gram-negative pathogens. Covalent protein cross-linking by an Asp-Lys isopeptide bond upon calcium-dependent processing at an Asp-Pro bond. *J Biol Chem* 279(24):24944–24956.
19. Sadilkova L, et al. (2008) Single-step affinity purification of recombinant proteins using a self-excising module from *Neisseria meningitidis* FrpC. *Protein Sci* 17(10):1834–1843.
20. Moradian-Oldak J, Leung W, Fincham AG (1998) Temperature and pH-dependent supramolecular self-assembly of amelogenin molecules: A dynamic light-scattering analysis. *J Struct Biol* 122(3):320–327.
21. Ravindranath HH, Chen LS, Zeichner-David M, Ishima R, Ravindranath RM (2004) Interaction between the enamel matrix proteins amelogenin and ameloblastin. *Biochem Biophys Res Commun* 323(3):1075–1083.
22. Mazumder P, Prajapati S, Lokappa SB, Gallon V, Moradian-Oldak J (2014) Analysis of co-assembly and co-localization of ameloblastin and amelogenin. *Front Physiol* 5:274.
23. Mazumder P, Prajapati S, Bapat R, Moradian-Oldak J (2016) Amelogenin-ameloblastin spatial interaction around maturing enamel rods. *J Dent Res* 95(9):1042–1048.
24. Bininda-Emonds OR, et al. (2007) The delayed rise of present-day mammals. *Nature* 446(7135):507–512.
25. Pyron RA, Wiens JJ (2011) A large-scale phylogeny of Amphibia including over 2800 species, and a revised classification of extant frogs, salamanders, and caecilians. *Mol Phylogenet Evol* 61(2):543–583.
26. Jones ME, et al. (2013) Integration of molecules and new fossils supports a Triassic origin for Lepidosauria (lizards, snakes, and tuatara). *BMC Evol Biol* 13:208.
27. Welker F, et al. (2015) Ancient proteins resolve the evolutionary history of Darwin's South American ungulates. *Nature* 522(7554):81–84.
28. Uversky VN, Dunker AK (2010) Understanding protein non-folding. *Biochim Biophys Acta* 1804(6):1231–1264.
29. Dyson HJ (2011) Expanding the proteome: Disordered and alternatively folded proteins. *Q Rev Biophys* 44(4):467–518.
30. Tompa P (2011) Unstructural biology coming of age. *Curr Opin Struct Biol* 21(3):419–425.
31. Forlino A, Marini JC (2016) Osteogenesis imperfecta. *Lancet* 387(10028):1657–1671.
32. He G, Dahl T, Veis A, George A (2003) Nucleation of apatite crystals in vitro by self-assembled dentin matrix protein 1. *Nat Mater* 2(8):552–558.
33. Moradian-Oldak J, Paine ML, Lei YP, Fincham AG, Snead ML (2000) Self-assembly properties of recombinant engineered amelogenin proteins analyzed by dynamic light scattering and atomic force microscopy. *J Struct Biol* 131(1):27–37.
34. Paine ML, et al. (2000) Enamel biomineralization defects result from alterations to amelogenin self-assembly. *J Struct Biol* 132(3):191–200.
35. Carneiro KM, et al. (2016) Amyloid-like ribbons of amelogenins in enamel mineralization. *Sci Rep* 6:23105.
36. Wazen RM, Moffatt P, Zalzal SF, Yamada Y, Nanci A (2009) A mouse model expressing a truncated form of ameloblastin exhibits dental and junctional epithelium defects. *Matrix Biol* 28(5):292–303.
37. Iwata T, et al. (2007) Processing of ameloblastin by MMP-20. *J Dent Res* 86(2):153–157.
38. Nagano T, et al. (2009) Mmp-20 and Klk4 cleavage site preferences for amelogenin sequences. *J Dent Res* 88(9):823–828.
39. Uchida T, et al. (1991) Immunochemical and immunohistochemical studies, using antisera against porcine 25 kDa amelogenin, 89 kDa enamelin and the 13-17 kDa nonamelogenins, on immature enamel of the pig and rat. *Histochemistry* 96(2):129–138.
40. Uchida T, et al. (1997) Synthesis, secretion, degradation, and fate of ameloblastin during the matrix formation stage of the rat incisor as shown by immunocytochemistry and immunochemistry using region-specific antibodies. *J Histochem Cytochem* 45(10):1329–1340.
41. Hu CC, et al. (1997) Sheathlin: Cloning, cDNA/polypeptide sequences, and immunolocalization of porcine enamel sheath proteins. *J Dent Res* 76(2):648–657.
42. Geng S, White SN, Paine ML, Snead ML (2015) Protein interaction between ameloblastin and proteasome subunit α type 3 can facilitate redistribution of ameloblastin domains within forming enamel. *J Biol Chem* 290(34):20661–20673.
43. Fukae M, Tanabe T (1987) 45Ca-labeled proteins found in porcine developing dental enamel at an early stage of development. *Adv Dent Res* 1(2):261–266.
44. Wood CB, Stern DN (1997) The earliest prisms in mammalian and reptilian enamel. *Tooth Enamel Microstructure*, eds Koenigswald W, Sander PM (A. A. Balkema, Rotterdam), pp 63–83.
45. Horacek I, Spoutil F (2012) Why tribosphenic? On variation and constraint in developmental dynamics of chiropteran molars. *Evolutionary History of Bats: Fossils, Molecules and Morphology*, eds Gunnell GF, Simmons NB (Cambridge Univ Press, Cambridge, UK), pp 572.
46. Sambrook J, Fritsch EF, Maniatis T (1989) *Molecular Cloning: A Laboratory Manual* (Cold Spring Harbor Laboratory, Cold Spring Harbor, NY) 2nd Ed.
47. Simmer JP, et al. (1994) Isolation and characterization of a mouse amelogenin expressed in *Escherichia coli*. *Calcif Tissue Int* 54(4):312–319.
48. Kasparek P, et al. (2014) Efficient gene targeting of the Rosa26 locus in mouse zygotes using TALE nucleases. *FEBS Lett* 588(21):3982–3988.
49. Reynolds ES (1963) The use of lead citrate at high pH as an electron-opaque stain in electron microscopy. *J Cell Biol* 17:208–212.
50. Robinson C, Kirkham J, Stonehouse NJ, Shore RC (1989) Control of crystal growth during enamel maturation. *Connect Tissue Res* 22(1-4):139–145.
51. Simmer JP, Hu Y, Lertlam R, Yamakoshi Y, Hu JC (2009) Hypomaturation enamel defects in Klk4 knockout/LacZ knockin mice. *J Biol Chem* 284(28):19110–19121.